



Observations of Solar Wind from Earth-directed Coronal Pseudostreamers

Y.-M. Wang¹ and O. Panasenco²

¹ Space Science Division, Naval Research Laboratory, Washington, DC 20375, USA; yi.wang@nrl.navy.mil

² Advanced Heliophysics, Pasadena, CA 91106, USA; panasenco.olga@gmail.com

Received 2018 December 18; revised 2019 January 14; accepted 2019 January 15; published 2019 February 19

Abstract

Low-speed ($\lesssim 450 \text{ km s}^{-1}$) solar wind is widely considered to originate from streamer loops that intermittently release their contents into the heliosphere, in contrast to high-speed wind, which has its source in large coronal holes. To account for the presence of slow wind far from the heliospheric current sheet (HCS), it has been suggested that “pseudostreamers” rooted between coronal holes of the same polarity continually undergo interchange reconnection with the adjacent open flux, producing a wide band of slow wind centered on the separatrix/plasma sheet that extends outward from the pseudostreamer cusp. Employing extreme-ultraviolet images and potential-field source-surface extrapolations, we have identified 10 Earth-directed pseudostreamers during 2013–2016. In situ measurements show wind speeds ranging from ~ 320 to $\sim 600 \text{ km s}^{-1}$ in the days immediately preceding and following the predicted pseudostreamer crossings, with the proton densities and O^{7+}/O^{6+} ratios tending to be inversely correlated with the bulk speed. We also identify examples of coronal holes that straddle the solar equator and give rise to wind speeds of order 400 km s^{-1} . Our results support the idea that the bulk of the slow wind observed more than a few degrees from the HCS originates from just inside coronal holes.

Key words: solar wind – Sun: activity – Sun: corona – Sun: heliosphere – Sun: magnetic fields – Sun: UV radiation

1. Introduction

While it has been recognized since the *Skylab* era of the 1970s that high-speed solar wind emanates from large coronal holes, the origin of wind with near-Earth speeds in the range $v \sim 300\text{--}450 \text{ km s}^{-1}$ remains an unresolved question (for a review, see Abbo et al. 2016). The now-prevailing view is that the slow wind is released from closed coronal loops that undergo “interchange” reconnection with nearby open magnetic flux, a scenario that attempts to account for its greater variability and differing composition (high charge-state ratios, enrichment in elements of low first-ionization potential relative to fast “coronal-hole” wind (see, e.g., Schwadron et al. 1999; Zurbuchen et al. 2000; Antiochos et al. 2011).

An alternative scenario is suggested by the inverse correlation between wind speed and the rate at which the underlying flux tube expands in the corona, as inferred from outward extrapolations of the measured photospheric field (Levine et al. 1977; Wang & Sheeley 1990; Arge & Pizzo 2000; Cohen 2015; Poduval 2016). According to this view, slow wind originates from rapidly diverging flux tubes rooted inside small coronal holes or just within the boundaries of large holes. This may be understood physically if the coronal heating rate is taken to depend on the local magnetic field strength. The effect of rapid flux-tube divergence is then to concentrate the heating near the coronal base, thereby increasing the mass flux but decreasing the energy per proton available to accelerate the wind; moreover, with the temperature maximum being located at lower heights, the freezing-in temperatures will be higher in slow wind than in fast wind, as observed (see Wang & Sheeley 2003; Cranmer et al. 2007; Wang et al. 2009).

That at least a small fraction of the slow wind comes from closed-field regions is indicated by white-light observations of streamer blobs and raylike fine structure in the immediate vicinity of the heliospheric current sheet (HCS). The blobs are actually small flux ropes formed when helmet streamer loops

reconnect with each other and pinch off (Sheeley et al. 2009; Rouillard et al. 2010), while the raylike appearance of the heliospheric plasma sheet may be the result of interchange reconnection between the streamer loops and the adjacent open flux (Wang et al. 1998). However, low-speed wind is often recorded far from interplanetary sector boundaries and is particularly ubiquitous around solar maximum, even where coronal mass ejections (CMEs) appear to be absent.

The streamer structure in the outer corona consists not only of helmet streamers, which are here defined as separating coronal holes of opposite polarity, but also of “pseudostreamers,” which separate coronal holes of the same polarity (see Eselevich et al. 1999; Wang et al. 2007, 2012; Crooker et al. 2012; Riley & Luhmann 2012; Panasenco & Velli 2013; Owens et al. 2014; Abbo et al. 2015; Panasenco et al. 2019). While lacking current sheets, pseudostreamers have plasma sheet extensions that outline a network of separatrices branching off from the HCS. These sheets again consist of raylike features that may be a product of interchange reconnection at the underlying X-point, which typically lies inside heliocentric radius $r \sim 2 R_{\odot}$. The adjacent open flux undergoes a nonmonotonic expansion, diverging rapidly between the coronal base and the X-point but then reconverging.

According to the “S-web” model of Antiochos et al. (2011), interchange reconnection gives rise to wide bands of slow wind that surround not only the HCS but also the pseudostreamer separatrices. Recent magnetohydrodynamic simulations have shown that, when large-amplitude circular motions are applied near coronal-hole boundaries, loops rooted outside the boundary may transfer their material to open field lines located far from the HCS (Higginson et al. 2017a, 2017b; Higginson & Lynch 2018). That the strong footpoint driving employed in the simulations is consistent with the actual photospheric flow field has yet to be demonstrated. The presence of turbulence or the fragmentation of the current layer where reconnection occurs

may also act to broaden the boundary between open and closed flux (Rappazzo et al. 2012; Pontin & Wyper 2015). Constraints on the actual width of the interface may be provided by the sharpness of coronal-hole boundaries seen in extreme-ultraviolet (EUV) and X-ray images, as well as by coronagraph observations of the heliospheric plasma sheet(s), which appear to be narrower than $\sim 3^\circ$ when viewed edge-on (see Figure 1 in Wang et al. 1998).

In the in situ solar wind, helmet streamer crossings are associated with interplanetary sector boundaries, whereas pseudostreamer crossings are assumed to occur near stream interfaces where the wind speed undergoes a rapid transition but the direction of the interplanetary magnetic field (IMF) does not reverse (see, e.g., Neugebauer et al. 2004). Applying a superposed epoch analysis to 128 such stream interfaces from the period 1998–2009, Crooker et al. (2014; see also Crooker & McPherron 2012) found that the wind on the leading, lower-speed side of the interface had properties similar to the slow wind around sector boundary crossings, but with the average speeds and charge-state ratios being somewhat higher. Using potential-field source-surface (PFSS) extrapolations, Crooker et al. (2014) also predicted the times of in situ pseudostreamer encounters. As illustrated by their Figure 2, multiple pseudostreamer crossings may sometimes occur within a single IMF polarity sector, none of which need coincide with the observed stream interface but may precede or follow it by $\sim 1\text{--}2$ days. There may be a number of reasons for the apparent mismatch. The uncertainty in the PFSS estimates may well be on the order of a day or more. In addition, some pseudostreamers may lack associated stream interfaces. As acknowledged by Crooker et al. (2014), the use of such interfaces to identify pseudostreamer flows selects out the subset of pseudostreamers having slow (fast) wind on their leading (trailing) side. If the wind speeds on the leading side are greater than or comparable to those on the trailing side, a stream interface may not necessarily form.

In an earlier study (Wang et al. 2012), we identified three in situ pseudostreamer crossings having associated stream interfaces, where the minimum wind speeds ranged from ~ 390 to $\sim 480 \text{ km s}^{-1}$, as well as a predicted crossing within a high-speed stream, where $v \sim 550 \text{ km s}^{-1}$. We concluded that the solar wind near pseudostreamers tends to have speeds and compositional properties intermediate between those of the slow wind near helmet streamers and the fast wind from the interiors of large coronal holes. To explore further the relationship between pseudostreamers and slow solar wind, we here examine several pseudostreamer crossings from the period 2013–2016, again employing EUV observations of coronal holes, PFSS extrapolations, and in situ wind data.

2. Procedure

To locate coronal pseudostreamers and their heliospheric extensions, we apply a PFSS extrapolation to Carrington maps of the photospheric field from the National Solar Observatory (NSO/SOLIS) and/or from the Wilcox Solar Observatory (WSO). With r denoting heliocentric distance, L heliographic latitude, and ϕ Carrington longitude, the magnetic field $\mathbf{B}(r, L, \phi)$ remains current-free from the coronal base to $r = R_{ss} = 2.5 R_\odot$, where B_L and B_ϕ are required to vanish; all field lines that cross the source surface are considered to be “open.” At $r = R_\odot$, B_r is matched to the photospheric field, assumed to be approximately radial at the depth where it is measured

(see Wang & Sheeley 1992). The WSO flux densities are corrected for the saturation of the Fe I 525.0 nm line profile by multiplying by the latitude-dependent factor ($4.5\text{--}2.5 \sin^2 L$) (Wang & Sheeley 1995).

Tracing downward from the source surface, we first determine the footpoint areas of open field lines, including those that intersect the ecliptic plane. We then verify that the predicted open field regions correspond to coronal holes appearing in synoptic maps of Fe XIV 21.1 nm intensity, which are constructed from Atmospheric Imaging Assembly (AIA) images from the *Solar Dynamics Observatory* (*SDO*). Pseudostreamer separatrices are located by comparing the footpoint positions of like-polarity open field lines that are spaced 2° apart at the source surface; if the angular separation of the footpoints exceeds 10° , the field lines are taken to lie on opposite sides of a separatrix.³ We remark that such separatrices may occur not only between two distinct coronal holes of the same polarity, but also between nonadjacent parts of the convoluted boundary of a single hole.

The factor by which an open flux tube expands in (Sun-centered) solid angle between the coronal base and radius r is given by

$$f(r) = \left(\frac{R_\odot}{r} \right)^2 \frac{B_0}{|B_r|}, \quad (1)$$

where B_0 denotes the footpoint field strength. Previous studies (e.g., Wang & Sheeley 1990; Arge & Pizzo 2000) have demonstrated that the solar wind speed at 1 au is inversely correlated with $f_{ss} \equiv f(R_{ss})$. However, this parameter overestimates the wind speed in the vicinity of pseudostreamers, where the open flux initially diverges rapidly but then reconverges (see Riley & Luhmann 2012; Wang et al. 2012; Panasenco & Velli 2013; Panasenco et al. 2019). To characterize the expansion rates of open field lines, we here employ the parameter f_{\max} , defined as the maximum value of $f(r)$ between $r = R_\odot$ and $r = R_{ss}$.

For comparisons with in situ data, we assume that the solar wind propagates radially from $r = 2.5 R_\odot$ to 1 au, with the transit time being inversely proportional to the observed near-Earth speed v . Hourly averages of v , proton density n_p , and IMF longitude angle ϕ_B relative to the Sun–Earth line are extracted from the OMNIWeb site,⁴ while two-hourly averages of O^{+}/O^{6+} are obtained from the *Advanced Composition Explorer* (*ACE*) SWICS 2.0 database.⁵ For consistency with the spatial/temporal resolution of our PFSS extrapolations, the data are smoothed by taking 10 hr running averages. The source locations of the near-Earth wind are found by tracing inward along the magnetic field, taking into account the longitude shift due to solar rotation.

3. Case Studies of Earth-directed Pseudostreamers

While helmet streamers (and their heliospheric extension in the form of the HCS) are often located close to the ecliptic plane, especially around solar minimum, the great majority of

³ The identification of separatrices is somewhat arbitrary and depends on the spatial resolution of the photospheric field measurements. The ubiquitous presence of small-scale, mixed-polarity flux inside coronal holes implies that the source surface is in fact crisscrossed by a much finer web of separatrices than that associated with the large-scale structures considered here.

⁴ See omniweb.gsfc.nasa.gov.

⁵ See www.srl.caltech.edu/ACE/ASC/level2.

large, long-lived pseudostreamers are centered at midlatitudes, where they separate the polar coronal holes from low-latitude holes of the same polarity. Pseudostreamers whose plasma sheets intersect the ecliptic tend to be rooted far from the solar equator or to be associated with relatively small, short-lived holes. Here we describe some unusually unambiguous examples of Earth-directed pseudostreamers that were sources of in-ecliptic solar wind during 2013–2016. The criteria used in selecting these cases included: (1) qualitative agreement between the observed and PFSS-derived coronal-hole boundaries; (2) no obvious CME signatures near the predicted pseudostreamer crossing; (3) to avoid confusion with helmet streamers, an angular separation of at least 20° between the in situ pseudostreamer location and the nearest interplanetary sector boundary (or HCS/source-surface neutral line).

3.1. Carrington Rotation (CR) 2136: 2013 April–May

We first consider the pseudostreamer systems associated with three coronal holes observed during CR 2136, near the maximum of solar cycle 24. Figure 1 displays (a) the global distribution of Fe XIV 21.1 nm emission, (b) the NSO photospheric field with the footpoint areas of open flux represented by colored dots, (c) the neutral line (white pixels) and pseudostreamer separatrices (gray pixels) at the source surface, and (d) the variation of v , ϕ_B , n_p , and O^{7+}/O^{6+} as a function of Carrington longitude ϕ . In the map of open field regions, the darker colors (blue, green) represent larger values of f_{\max} , while the warmer colors (yellow, orange) denote smaller values; the colored diamonds (similarly coded and plotted also on the source-surface map) indicate the maximum expansion factors of flux tubes connected to the ecliptic plane, with white lines linking their ecliptic positions to their photospheric footpoints. The solar wind data in the bottom panel are plotted in time-reversed order; note also that mapping the wind back to the source surface using a time lag proportional to v^{-1} alters the relative longitudinal extents of the leading and trailing portions of a given stream, steepening the latter but stretching the former.

The EUV map (Figure 1(a)) shows a northern-hemisphere hole near $\phi \sim 270^\circ$ and a large southern-hemisphere coronal hole extending over the longitude range $\sim 275^\circ$ – 325° . The corresponding open field regions are rooted in negative-polarity photospheric flux (Figure 1(b)) and give rise to a separatrix system that intersects the ecliptic plane near longitude 300° (Figure 1(c)). At $\phi \sim 210^\circ$ and $L \sim +10^\circ$, a small northern-hemisphere hole of negative polarity may be seen to the east of the one near $\phi \sim 270^\circ$; the separatrix between the pair of like-polarity holes runs in the north–south direction and crosses the ecliptic at $\phi \sim 235^\circ$.

In the plot of near-Earth solar wind (Figure 1(d)), the vertical dashed lines mark the approximate locations of the two pseudostreamers. In both cases, the pseudostreamer crossing occurs on the westward (leading in time) side of a well-defined stream. The wind speeds observed during these encounters are $\sim 400 \text{ km s}^{-1}$ (at $\phi \sim 235^\circ$) and ~ 450 – 500 km s^{-1} (at $\phi \sim 300^\circ$), while the O^{7+}/O^{6+} ratios are on the order of 0.1–0.2. (Values of $O^{7+}/O^{6+} \lesssim 0.1$ have a factor of ~ 2 uncertainty.) It should be noted that the narrow plasma sheet extensions of pseudostreamers, whose properties may well differ from those of the adjacent coronal-hole wind, may no longer be clearly

identifiable at 1 au, where most of the local density enhancements are likely to be the result of stream interactions.

In obtaining these results, we have applied a PFSS extrapolation to NSO/SOLIS measurements of the photospheric field. Figure 2 shows the effect of replacing the NSO map, which has pixel dimensions of 360×180 , with a low-resolution (72×30) WSO map. Not surprisingly, even though the global configurations are similar, the open field regions and pseudostreamer separatrices derived from the WSO measurements exhibit considerably less fine structure than their NSO counterparts, with the WSO coronal holes tending to be larger and less fragmented. The predicted locations of the pseudostreamer separatrices typically differ by $\sim 5^\circ$ – 10° , providing a lower bound on the uncertainties associated with the magnetograph measurements.

As may be seen from Figure 2(d), the in-ecliptic pseudostreamer crossings predicted by the WSO extrapolations again occur on the leading sides of the wind streams of 2013 April 26 and May 2. Near these locations, where $v \sim 400$ – 500 km s^{-1} , the O^{7+}/O^{6+} ratio shows local maxima on the order of 0.2.

From Figures 1(c)–(d) and 2(c)–(d), we note that the expansion factors derived from both the NSO and the WSO measurements are relatively low ($f_{\max} < 9$: yellow and orange diamonds) in the vicinity of the moderately high-speed streams at $\phi \sim 140^\circ$ and $\phi \sim 280^\circ$, as expected from the inverse correlation between wind speed and expansion factor.

3.2. CR 2155: 2014 September–October

Figure 3 displays the distribution of Fe XIV intensity during CR 2155, the WSO photospheric field with the footpoint areas of open flux overplotted, the distribution of separatrices at the source surface, and the variation of the in-ecliptic solar wind as a function of Carrington longitude. (No NSO/SOLIS map is available for this CR.) The 21.1 nm map (Figure 3(a)) shows a near-equatorial hole around $\phi \sim 280^\circ$, which lies to the southeast of a fragmented, north–south oriented hole in the northern hemisphere. The corresponding open field regions both have positive polarity (Figure 3(b)) and are divided by a separatrix that crosses the ecliptic at $\phi \sim 325^\circ$ (Figure 3(c)). Although v is only on the order of 400 km s^{-1} at the time of the predicted pseudostreamer encounter, the O^{7+}/O^{6+} ratios are as low as ~ 0.05 ; this would imply a coronal-hole origin for the wind according to the criterion of Zhao et al. (2009), where 0.145 is the threshold value separating coronal hole from noncoronal hole wind.

The extended interval of low-speed (~ 370 – 450 km s^{-1}) wind centered on the equatorial coronal hole near $\phi \sim 280^\circ$ (date of central meridian passage: 2014 September 23) provides unusually clear support for the claim that coronal holes can be a major source of slow wind (see, e.g., Wang 2017). The PFSS extrapolation (Figures 3(b) and (c)) confirms that open field lines rooted inside the hole were connected to the ecliptic during this period, with their divergence rates having the high values ($f_{\max} > 9$: green and blue diamonds) associated with slow to moderately slow wind. The O^{7+}/O^{6+} ratios recorded during the passage of this hole ranged from ~ 0.05 to ~ 0.2 (Figure 3(d)).

3.3. CR 2174: 2016 February–March

During the declining phase of the sunspot cycle, when the global field configuration approximates that of a tilted dipole, the

NSO 2136 (2013 APRIL 17 - MAY 15)

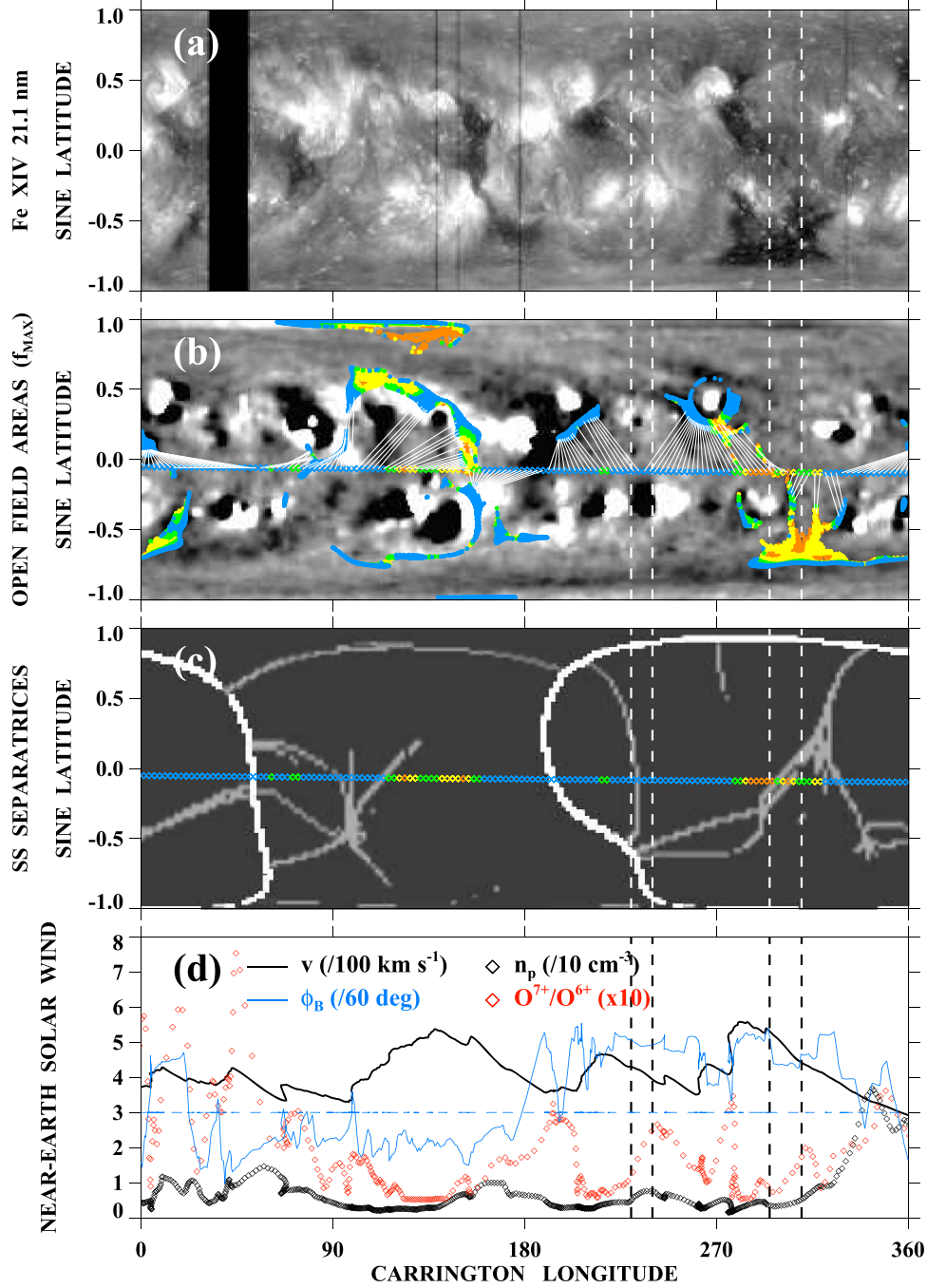


Figure 1. Observed and predicted coronal holes, open flux separatrices, and near-Earth solar wind as a function of Carrington longitude ϕ during CR 2136 (2013 April–May). Vertical dashed lines bracket the predicted source-surface positions of two Earth-directed pseudostreamers. (a) Distribution of Fe XIV 21.1 nm intensity recorded by *SDO/AIA*. (b) NSO/SOLIS photospheric field (saturated at $B_r = \pm 10$ G) with PFSS-derived open field regions overplotted as colored dots. Colored diamonds (plotted in the ecliptic plane) indicate the source-surface longitudes of Earth-directed flux tubes, with white lines connecting them to their photospheric footpoints. Here and in subsequent figures, dots and diamonds are color-coded as follows: blue ($f_{\max} > 18$); green ($9 < f_{\max} < 18$); yellow ($4 < f_{\max} < 9$); and orange ($f_{\max} < 4$). (c) Boundaries/separatrices between open flux domains at $r = R_{ss} = 2.5 R_{\odot}$, with white pixels marking the neutral line (HCS) and gray pixels representing pseudostreamer locations. Colored diamonds again indicate the maximum expansion factors of Earth-directed flux tubes. (d) Variation of the near-Earth wind speed v , proton density n_p , and O^{7+}/O^{6+} ratio as a function of ϕ . Also plotted is the IMF longitude angle ϕ_B , measured counterclockwise from the Sun–Earth line and lying in the quadrant 90° – 180° (270° – 360°) if the IMF points away from (toward) the Sun. (Horizontal dashed line marks $\phi_B = 180^\circ$.) The OMNI and ACE/SWICS measurements have been smoothed by taking 10 hr running means, and have been mapped back to the source surface assuming a transit time $\propto v^{-1}$. Values of $O^{7+}/O^{6+} \lesssim 0.1$ are uncertain by factors of order 2. Near the predicted pseudostreamer crossings ($\phi \sim 235^\circ$ and $\phi \sim 300^\circ$), $v \sim 400$ – 500 km s $^{-1}$ and $O^{7+}/O^{6+} \sim 0.1$ – 0.2 .

polar coronal holes may be highly nonaxisymmetric, often showing large, off-axis lobes or long extensions that connect to low-latitude active regions (ARs). The equatorward extensions

sometimes take the form of narrow structures that maintain a vertical orientation from one rotation to the next; well-known examples include “Coronal Hole 1” of 1973 (Timothy et al. 1975)

WSO 2136 (2013 APRIL 17 - MAY 15)

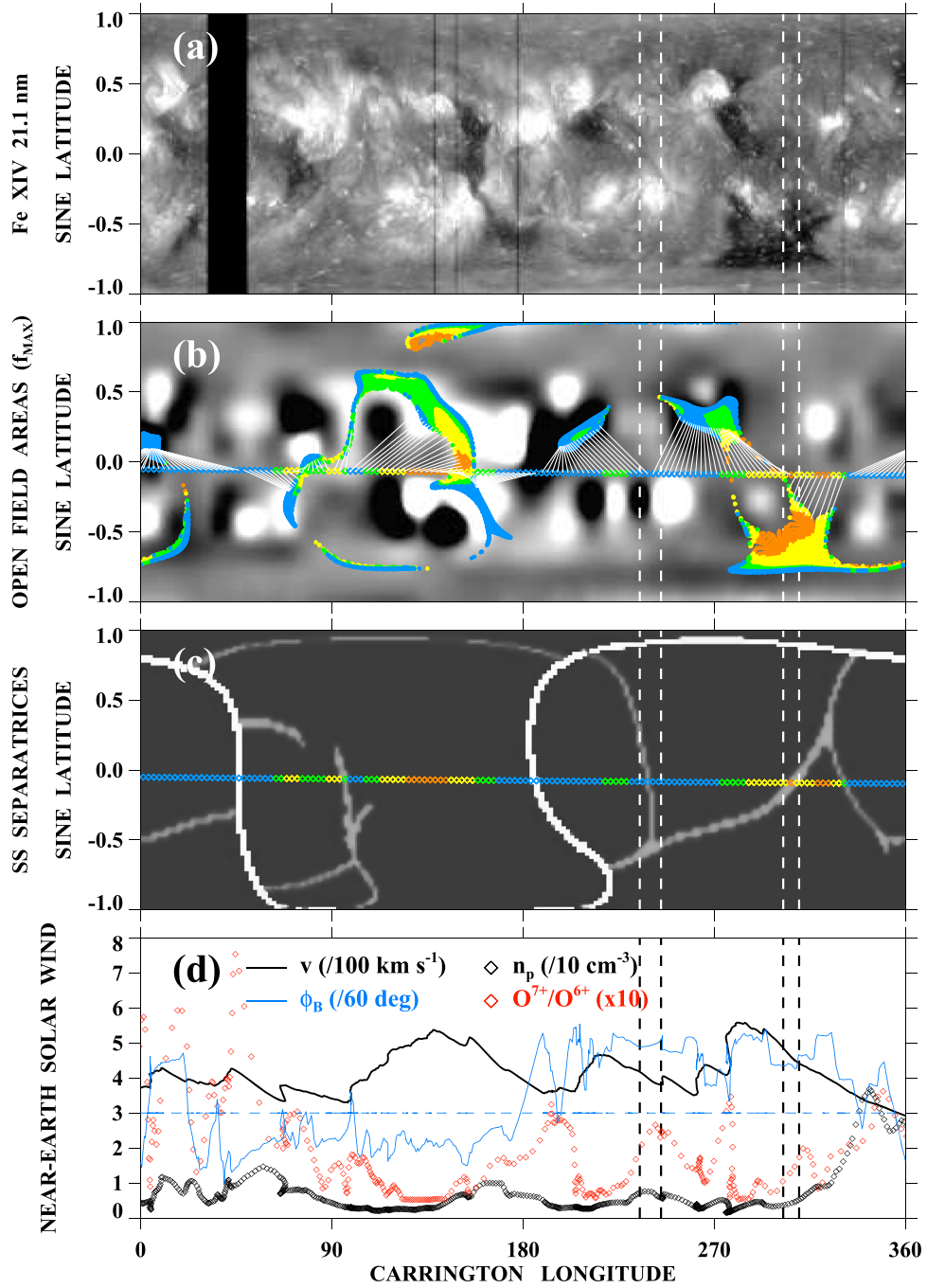


Figure 2. Same as in Figure 1, but with the NSO photospheric field map for CR 2136 replaced by a WSO map, which has pixel dimensions of 72×30 instead of 360×180 . Not surprisingly, the open field regions and separatrices derived from the low-resolution WSO measurements show less fine structure than those derived from the NSO measurements, although the basic patterns are similar. The predicted locations of the separatrices at the source surface differ by up to $\pm 10^\circ$ (~ 1 day). At the pseudostreamer crossings marked by pairs of vertical dashed lines, Figure 2(d) indicates wind speeds of $\sim 400\text{--}500 \text{ km s}^{-1}$ and $O^{7+}/O^{6+} \sim 0.1\text{--}0.25$.

and the “Elephant’s Trunk” of 1996 (Del Zanna & Bromage 1999; Zhao et al. 1999). The equatorward extension rotates quasi-rigidly at the rate of the low-latitude AR, a process that requires continual reconnection at the overlying helmet streamer cusp (Wang & Sheeley 1993, 2004).

Figure 4(a) shows the distribution of 21.1 nm emission during CR 2174. A vertical extension of the north polar hole may be seen at $\phi \sim 245^\circ$ (central meridian passage 2016 February 26), which terminates near an AR complex in the

southern hemisphere. A corresponding structure, embedded in a positive-polarity region extending from the north pole to well beyond $L \sim -30^\circ$, appears in the map of open field areas derived from the WSO photospheric field (Figure 4(b)). According to the PFSS extrapolation, this narrow transequatorial hole is connected to the ecliptic over the longitude range $\sim 210^\circ\text{--}280^\circ$. Figure 4(d) shows a clearly defined wind stream at this location; somewhat surprisingly, its peak speed is only on the order of 450 km s^{-1} . These rather low velocities are

WSO 2155 (2014 SEPTEMBER 17 - OCTOBER 14)

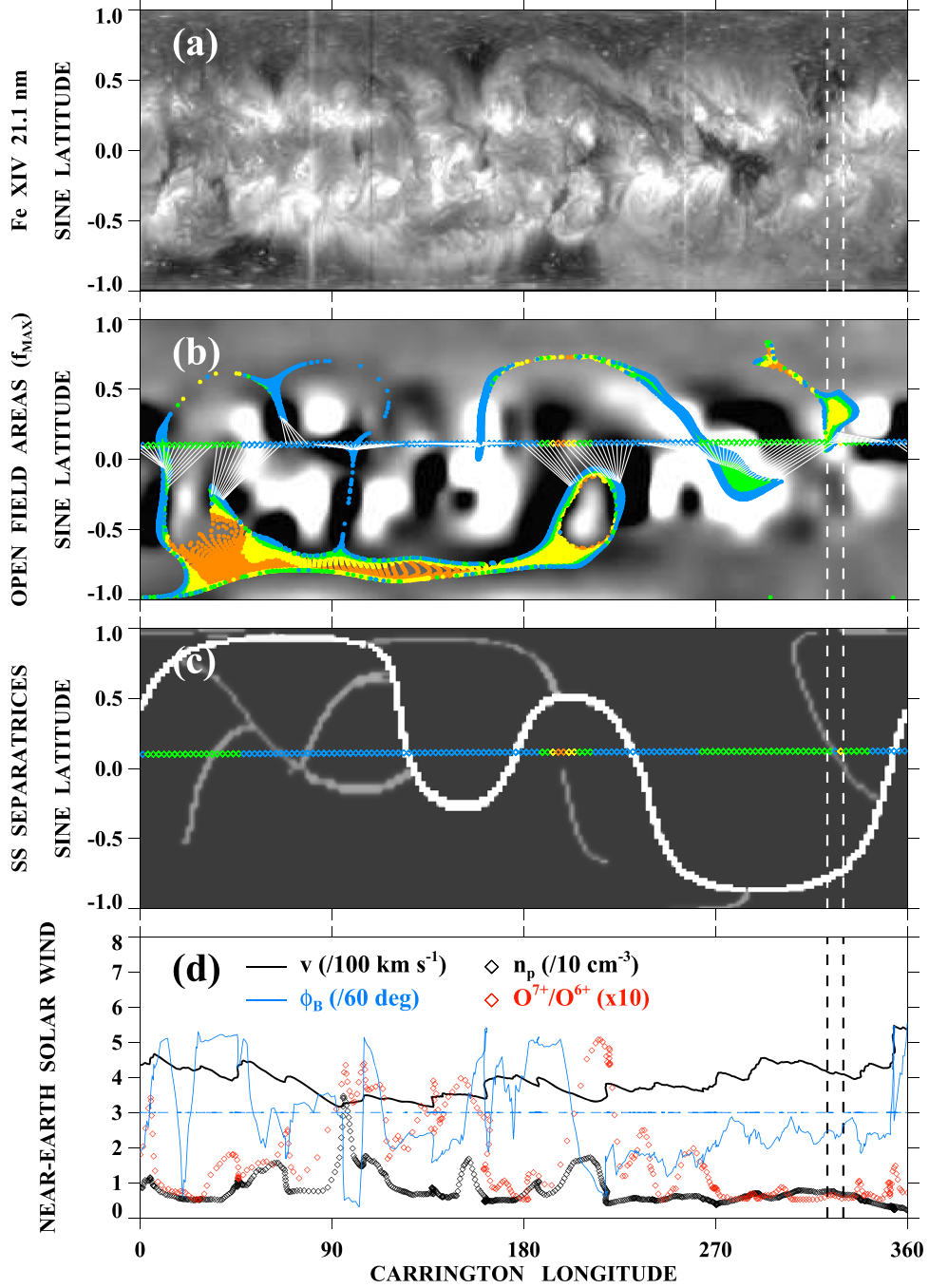


Figure 3. Observed and predicted coronal holes, separatrices, and near-Earth solar wind during CR 2155 (2014 September–October). (a) Distribution of Fe XIV 21.1 nm emission. (b) WSO photospheric field (saturated at \$B_r = \pm 10\$ G) with PFSS-derived open field regions overplotted. Diamonds indicate source-surface longitudes of Earth-directed flux tubes. Colors correspond to different ranges of the expansion factor \$f_{\max}\$ (as in Figure 1 caption). (c) Boundaries between open flux domains at \$r = R_{ss}\$, with white (gray) pixels representing the neutral line (pseudostreamer separatrices). (d) Variation of \$v\$, \$\phi_B\$, \$n_p\$, and \$\text{O}^{7+}/\text{O}^{6+}\$ as a function of Carrington longitude. During this period, the ecliptic is dominated by slow wind. At the predicted pseudostreamer crossing near longitude 325° (marked by the vertical dashed lines), \$v \sim 400 \text{ km s}^{-1}\$ and \$\text{O}^{7+}/\text{O}^{6+} \sim 0.05\$. Even the wind originating from inside the equatorial coronal hole near \$\phi \sim 280^\circ\$ shows speeds of only \$\sim 370\$–\$450 \text{ km s}^{-1}\$, with \$\text{O}^{7+}/\text{O}^{6+} \sim 0.05\$–\$0.2\$; the low speeds are consistent with the high values of \$f_{\max} (> 9)\$ indicated by the green and blue diamonds in (b) and (c).

consistent with the relatively large expansion factors (\$f_{\max} > 9\$: green and blue diamonds in Figures 4(b)–(c)) of the Earth-directed flux tubes.

To the west of the transequatorial extension, the north polar hole shows a broad equatorward bulge. The separatrix that divides this protuberance from the transequatorial hole extends

into the southern hemisphere, intersecting the ecliptic plane at \$\phi \sim 280^\circ\$ (see Figures 4(b) and (c)). The predicted position of the pseudostreamer coincides with an interface between the low-speed wind from the edge of the protuberance and the low-speed wind from the edge of the transequatorial hole. At this interface, \$v\$ falls to a minimum value of \$\sim 320 \text{ km s}^{-1}\$ and

WSO 2174 (2016 FEBRUARY 18 - MARCH 16)

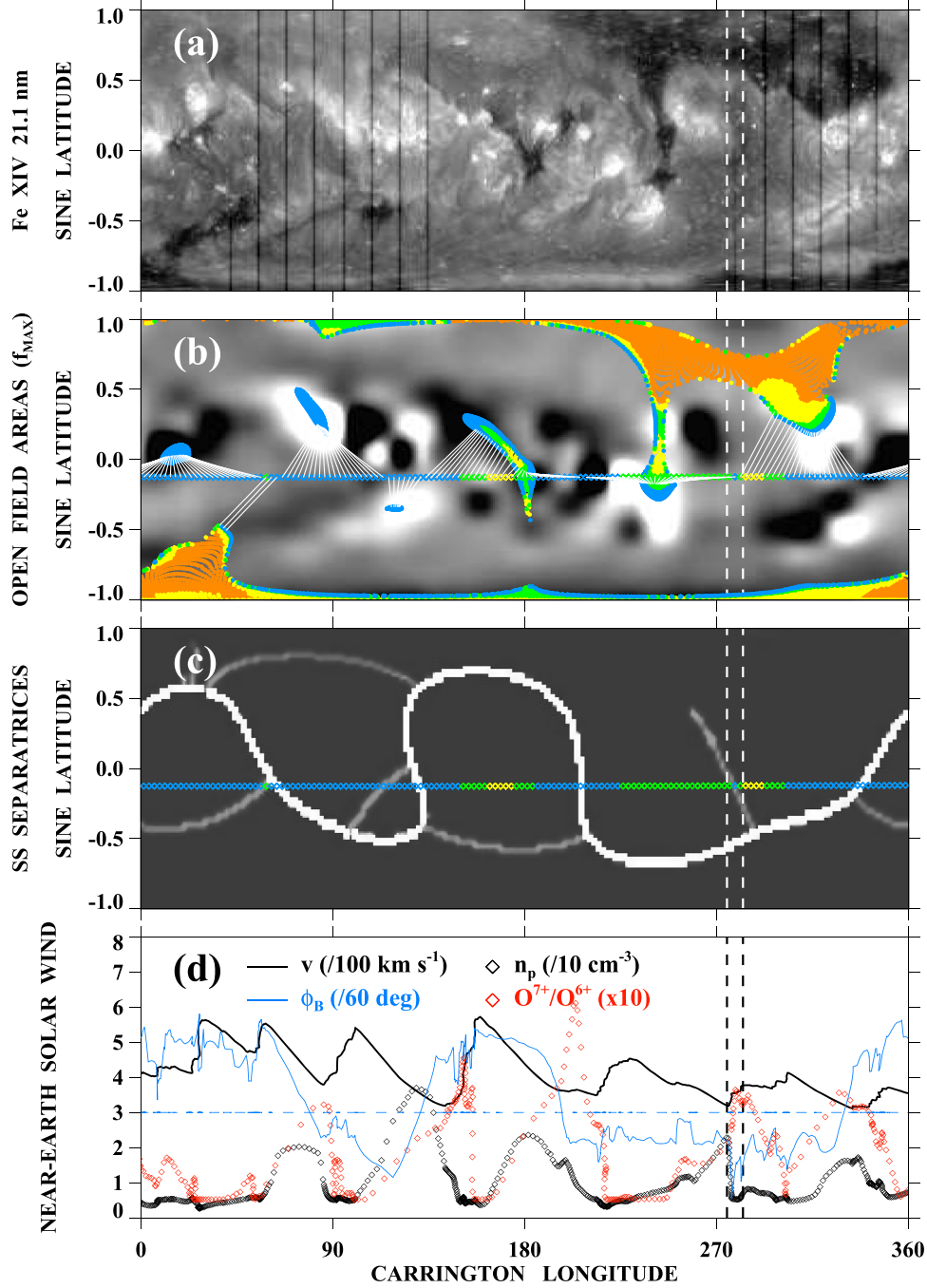


Figure 4. Identification of pseudostreamer separatrices during CR 2174 (2016 February–March). (a) Distribution of Fe XIV 21.1 nm intensity. (b) WSO photospheric field with PFSS-derived open field regions overplotted. (c) Boundaries between open flux domains at the source surface. (d) Near-Earth solar wind measurements. Symbols and color coding as in Figure 1. The transequatorial extension of the north polar hole, located near longitude 245° , is the source of an ecliptic wind stream with a peak speed of only $\sim 450 \text{ km s}^{-1}$. The separatrix between this narrow vertical extension and the western spur of the north polar hole intersects the ecliptic at $\phi \sim 280^\circ$. The predicted pseudostreamer crossing coincides with a stream interface where v dips to a minimum value of $\sim 320 \text{ km s}^{-1}$ and O^{7+}/O^{6+} peaks at ~ 0.35 .

O^{7+}/O^{6+} rises to ~ 0.35 . It is possible that the local density peak in this case may include a contribution from the original pseudostreamer plasma sheet.

3.4. CR 2178: 2016 June–July

Figure 5 displays, for CR 2178, the distribution of 21.1 nm intensity, the NSO photospheric field with open field regions superposed, the separatrices at the source surface, and the solar

wind variation near Earth. The Fe XIV map (Figure 5(a)) shows a large lobe of the north polar hole centered near $\phi \sim 270^\circ$, with two main equatorward-pointing arms. The open flux from each arm encounters its like-polarity counterpart above the intervening closed-field region (Figure 5(b)), forming a pseudostreamer separatrix that intersects the ecliptic near longitude 290° (Figure 5(c)). The point of intersection lies between two local maxima in the wind speed, where v falls to $\lesssim 500 \text{ km s}^{-1}$ and $O^{7+}/O^{6+} \sim 0.1$.

NSO 2178 (2016 JUNE 6 - JULY 3)

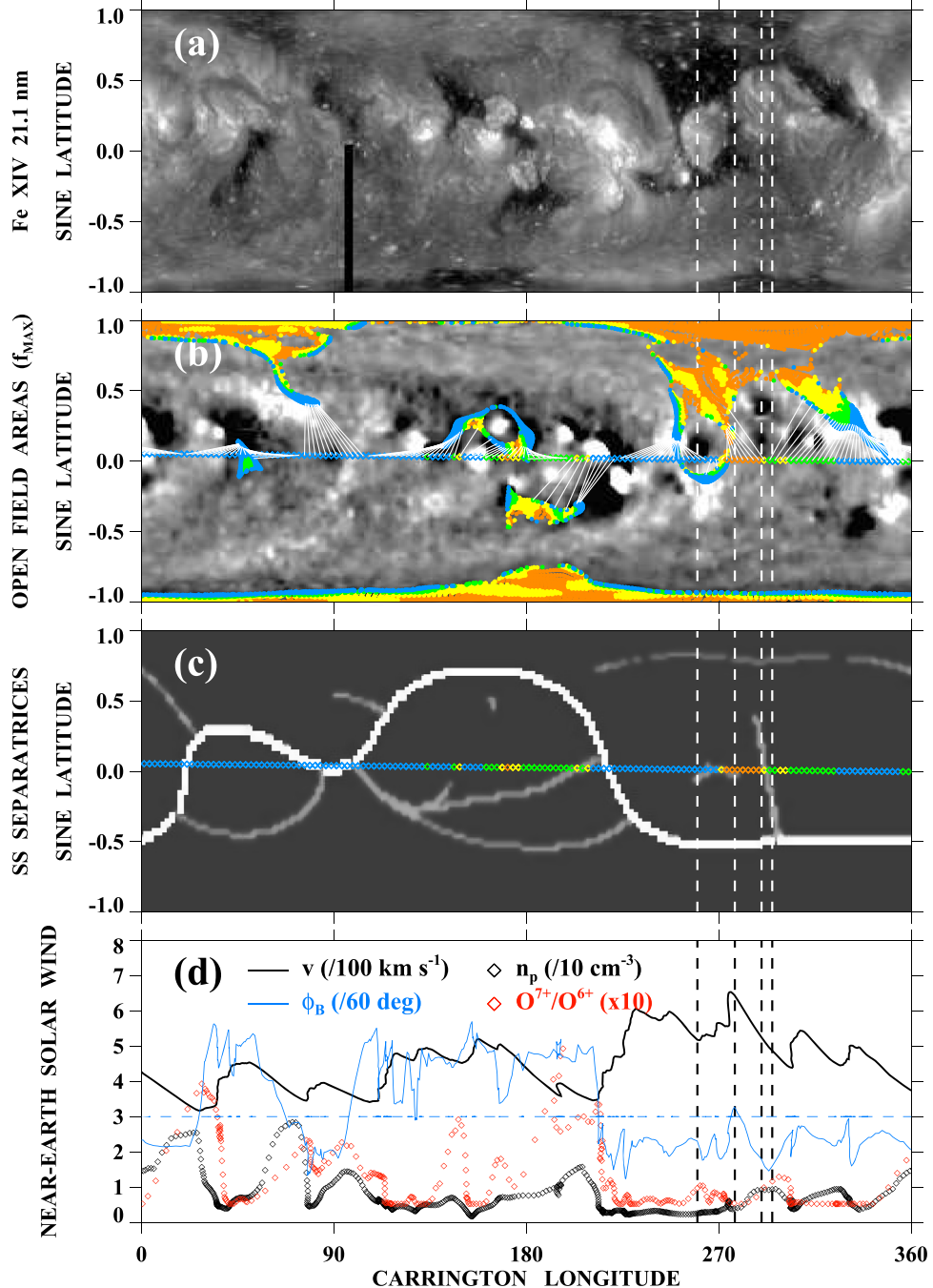


Figure 5. Identification of pseudostreamer separatrices during CR 2178 (2016 June–July). (a) Distribution of Fe XIV 21.1 nm intensity. (b) NSO photospheric field with open field regions overplotted. (c) Boundaries between open flux domains at $r = R_{ss}$. (d) Near-Earth solar wind measurements. Symbols and color coding as in Figure 1. The transequatorial hole near longitude 265° contains an AR remnant that gives rise to an isolated pseudostreamer (giant “plume”) near the ecliptic plane. At the corresponding position in the solar wind plot, the high-speed stream shows a dip, with v decreasing from $\gtrsim 600$ to $\lesssim 550 \text{ km s}^{-1}$ and O^{7+}/O^{6+} increasing from ~ 0.05 to ~ 0.1 . (This velocity dip may also be interpreted as an interface between two high-speed streams.) At $\phi \sim 290^\circ$, the Earth encounters another pseudostreamer, which is connected to the HCS and which separates the transequatorial hole from the western arm of the north polar hole; here, $v \sim 500 \text{ km s}^{-1}$ and $O^{7+}/O^{6+} \sim 0.1$.

The eastern arm of the polar-hole lobe contains an AR remnant at $\phi \sim 265^\circ$, which forms a circular area of closed field bordered by open flux (Figure 5(b)).⁶ The large pocket of

negative-polarity flux within the positive-polarity coronal hole effectively gives rise to a giant coronal plume, in which the surrounding open field lines converge above the X-point to form an isolated, axisymmetric pseudostreamer (Figures 6(a)–(b)). As may be seen from Figure 5(c), the separatrix associated with this pseudostreamer is not connected (to within the spatial resolution of the extrapolation) to the network that branches off the HCS/source-surface neutral line. As indicated by the

⁶ The eastern arm evolved from the narrow transequatorial extension appearing in Figure 4(a) and discussed in the previous subsection. The restructuring of the hole boundaries is mainly due to the emergence of NOAA 12532 at $L \sim +6^\circ$ during 2016 April.

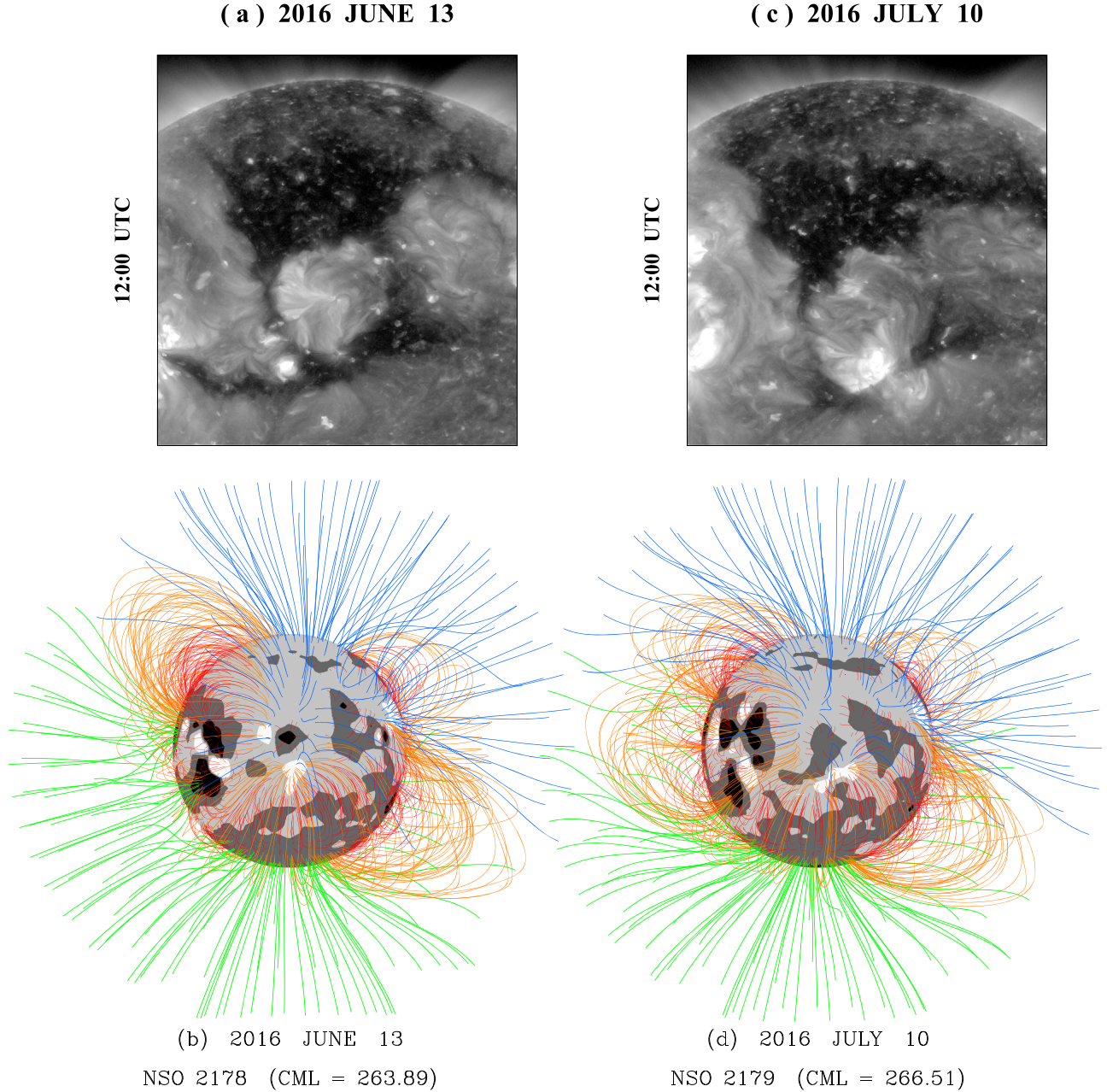


Figure 6. Plume-like pseudostreamer inside an equatorward extension of the north polar hole. (a) Fe XIV 21.1 nm image recorded at 12:00 UTC on 2016 June 13. (b) Corresponding coronal field-line configuration, derived from a PFSS extrapolation of NSO photospheric field measurements during CR 2178. (c) Fe XIV 21.1 nm image recorded at 12:00 UTC on 2016 July 10. (d) Coronal field-line configuration derived from the NSO photospheric field map for CR 2179. In the field-line plots, blue (green) denotes outward- (inward-) directed open flux; closed loops are orange if they extend above $r = 1.5 R_{\odot}$, red otherwise. Grayscale contours for the photospheric field range from black ($B_r < -10$ G) to white ($B_r > +10$ G). During CR 2178, the open flux within the equatorward extension completely surrounds the minority-polarity area near the equator, forming an isolated, axisymmetric pseudostreamer or large-scale “plume.” During CR 2179, however, some of the open flux alongside the pseudostreamer/plume closes down. Correspondingly, as shown by Figure 7(c), the pseudostreamer separatrix becomes connected to the network branching off the HCS.

vertical dashed lines at $\phi \sim 270^\circ$ in Figure 5(d), the pseudostreamer/plume is located near a local minimum in a high-speed stream (or an interface between two such streams); here, v dips to $\sim 500\text{--}550 \text{ km s}^{-1}$ and $O^{7+}/O^{6+} \sim 0.05\text{--}0.1$.

3.5. CR 2179: 2016 July

The plume-like pseudostreamer in Figures 5 and 6(a)–(b) was isolated from the rest of the network of separatrices because its base was surrounded by open flux of the same polarity. However, one rotation later (CR 2179), the narrow

corridors of open flux on the east and west sides of the “plume” have partially closed down and the 21.1 nm dark lanes have begun to fill in (see Figures 6(c)–(d) and Figures 7(a)–(b)). Correspondingly, as shown in Figure 7(c), pseudostreamer separatrices have now formed between the northern and southern parts of the polar-hole extension, as well as between each of these regions and the western arm of the polar-hole lobe; the three separatrices intersect near the ecliptic plane at $\phi \sim 285^\circ$ and are connected to the HCS. The in situ data (Figure 7(d)) show moderately fast wind over the entire

NSO 2179 (2016 JULY 3 - JULY 30)

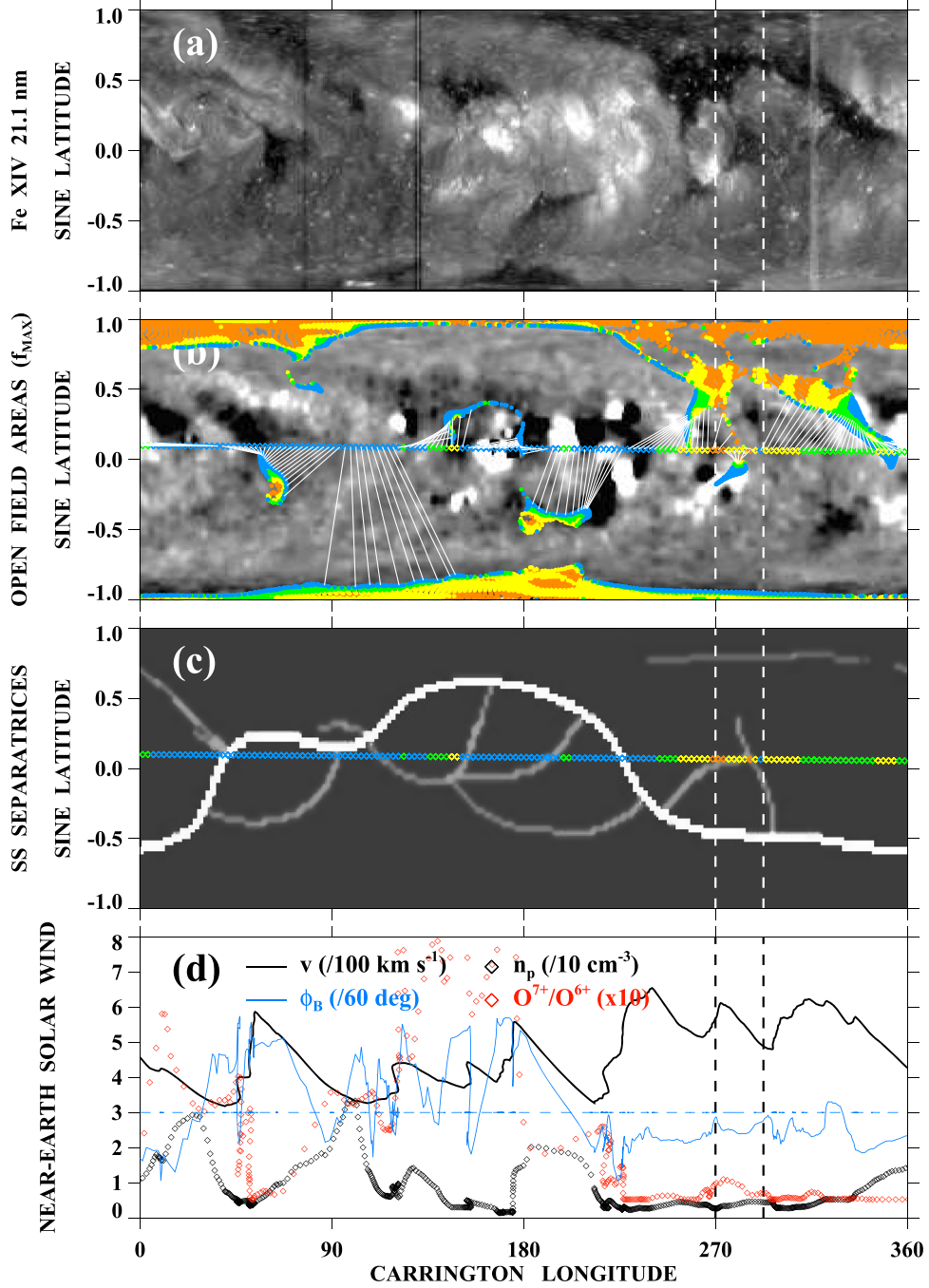


Figure 7. Pseudostreamer separatrices during CR 2179 (2016 July). (a) Distribution of Fe XIV 21.1 nm intensity. (b) NSO photospheric field with open field regions overplotted. (c) Boundaries between open flux domains at $r = R_{ss}$. (d) Near-Earth solar wind measurements. Symbols and color coding as in Figure 1. As the east and west sides of the transequatorial coronal hole begin to fill in and close down, the associated pseudostreamer becomes connected to the HCS and to the separatrix that divides the eastern and western arms of the north polar-hole lobe. The merged pseudostreamer system intersects the ecliptic near $\phi \sim 280^\circ$, where $v \sim 550 \text{ km s}^{-1}$ and $O^{7+}/O^{6+} \lesssim 0.1$.

longitude range $\sim 225^\circ$ – 350° ; in the region where the pseudostreamers intersect the ecliptic, $v \sim 500$ – 600 km s^{-1} and $O^{7+}/O^{6+} \lesssim 0.1$.

3.6. CR 2182: 2016 September–October

Figure 8 displays the distribution of Fe XIV 21.1 nm emission during CR 2182, the footpoint areas of open flux overplotted on the WSO photospheric field for this CR, the

separatrices between open field regions at the source surface, and the solar wind variation near Earth. At longitudes $\phi \sim 260^\circ$ – 320° , the EUV map (Figure 8(a)) shows a long extension of the north polar-hole lobe, which crosses the equator and then bends southeastward, penetrating well into the southern hemisphere (to latitude $L \sim -20^\circ$). This southern-hemisphere extension is separated from the northern-hemisphere lobe by a large area of diffuse emission, where the field is mainly closed (Figure 8(b)). Correspondingly, the source-

WSO 2182 (2016 SEPTEMBER 23 - OCTOBER 20)

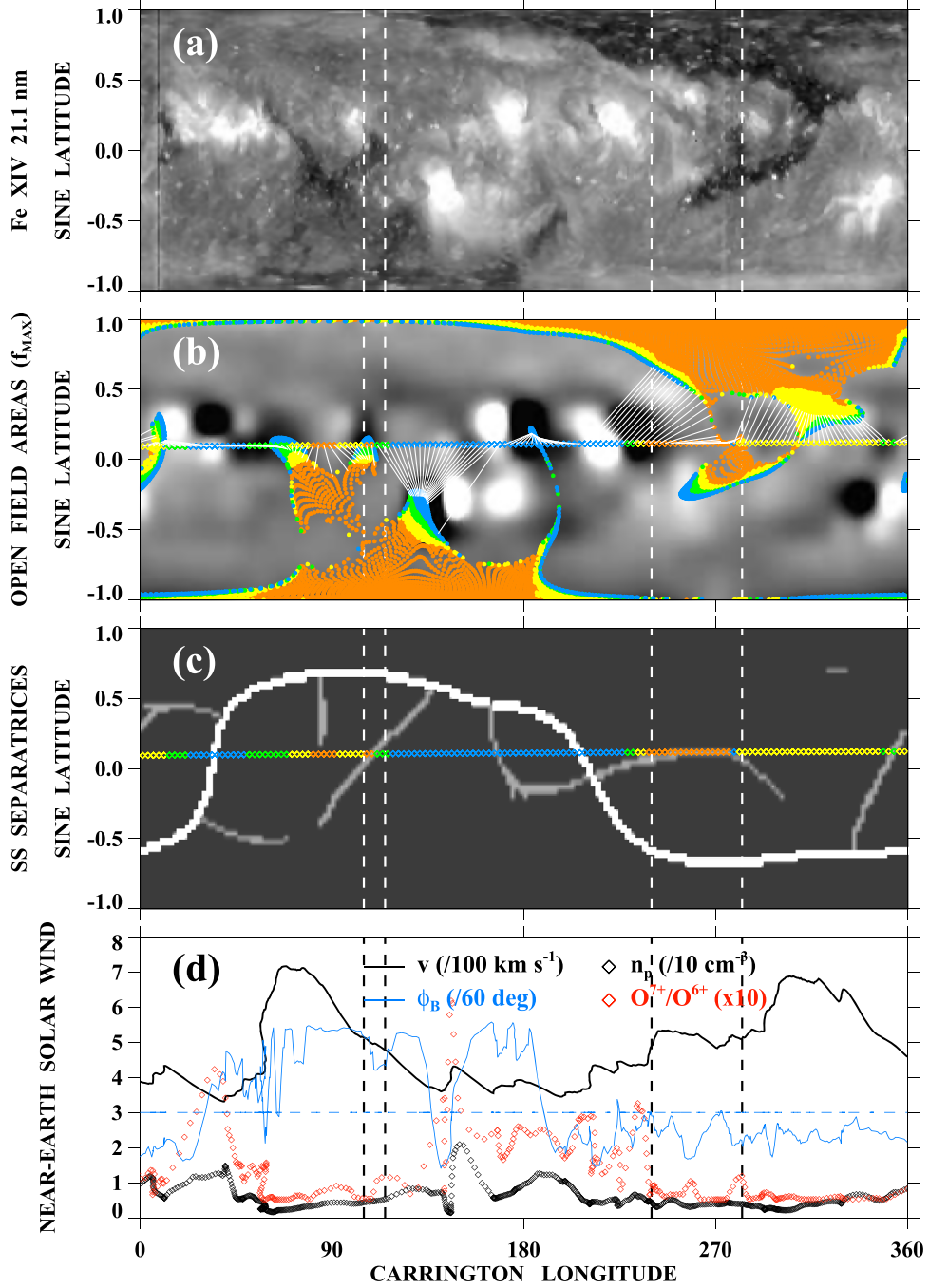


Figure 8. Identification of pseudostreamer separatrices during CR 2182 (2016 September–October). (a) Distribution of Fe XIV 21.1 nm intensity. (b) WSO photospheric field with open field regions overplotted. (c) Boundaries between open flux domains at $r = R_{ss}$. (d) Near-Earth solar wind measurements. Symbols and color coding as in Figure 1. The transequatorial extension of the north polar-hole lobe bends southeastward below the equator, giving rise to a pseudostreamer separatrix that runs along the ecliptic over the longitude range $\sim 240^\circ$ – 280° . The wind speeds recorded during this interval remain close to 500 km s^{-1} , with $O^{7+}/O^{6+} \sim 0.05$ – 0.1 . Farther to the east, two spurs of the south polar-hole lobe are separated by a pseudostreamer that crosses the ecliptic near longitude 110° . At this location, the solar wind plot shows a small shoulder in the wind speed, where again $v \sim 500 \text{ km s}^{-1}$ and $O^{7+}/O^{6+} \sim 0.05$ – 0.1 .

surface map (Figure 8(c)) shows a pseudostreamer separatrix that runs roughly in the east–west direction and becomes tangential to the ecliptic plane over the longitude range $\sim 240^\circ$ – 280° . Here, $v \sim 500 \text{ km s}^{-1}$ and $O^{7+}/O^{6+} \sim 0.05$ – 0.1 (Figure 8(d)). At longitudes $\lesssim 240^\circ$, as v falls toward $\sim 400 \text{ km s}^{-1}$ and below, the charge-state ratios increase and fluctuate between ~ 0.1 and ~ 0.3 . According to Figure 8(b), the

near-Earth wind during this latter period originates from the outer edge of the north polar-hole lobe.

At $\phi \sim 110^\circ$ in Figure 8, the vertical dashed lines mark another predicted pseudostreamer crossing. Here, the ecliptic-intersecting separatrix divides two equatorward spurs of the south polar-hole lobe. The wind speeds in the vicinity of the crossing are again on the order of 500 km s^{-1} , while $O^{7+}/O^{6+} \sim 0.05$ – 0.1 .

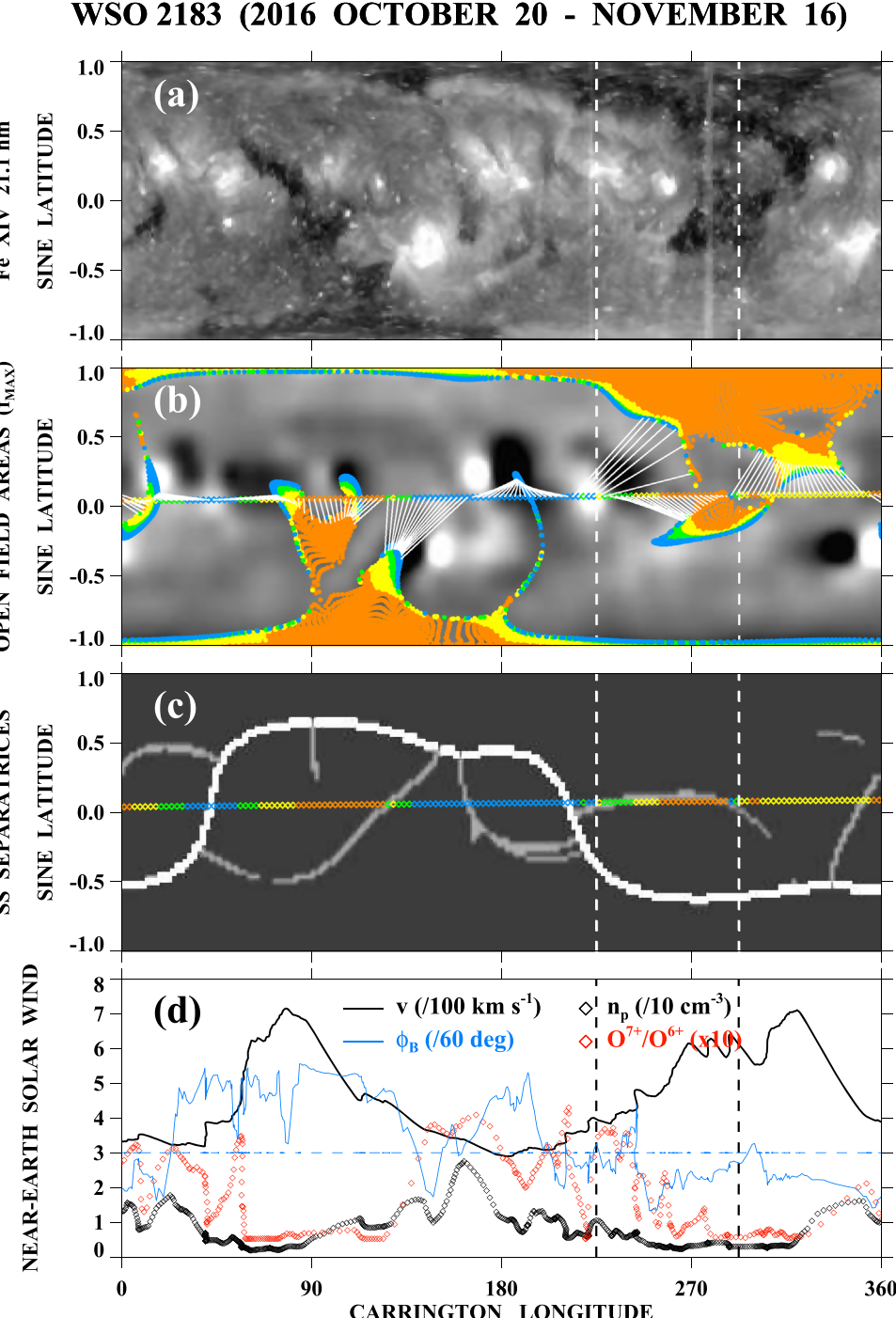


Figure 9. Distribution of 21.1 nm emission, open field regions derived from the WSO photospheric field, separatrices at the source surface, and solar wind measurements for CR 2183 (2016 October–November). The PFSS extrapolation again predicts an extensive in situ encounter, over the longitude range $\sim 225^\circ$ – 290° , with the pseudostreamer associated with the transequatorial extension of the north polar hole. At longitudes $\phi \sim 270^\circ$ – 290° , where the underlying coronal hole has widened, the wind speed has increased from ~ 500 to ~ 600 km s⁻¹ (compare Figure 8). However, at longitudes $\lesssim 245^\circ$, where v falls to ~ 400 km s⁻¹, O^{7+}/O^{6+} and the IMF angle undergo increased fluctuations. A possible source of these fluctuations is the small emerging AR located at $\phi \sim 260^\circ$ in the Fe XIV map (see also Figure 10).

3.7. CR 2183: 2016 October–November

Figure 9 shows the observed and predicted coronal holes, source-surface separatrices, and in situ solar wind during CR 2183. Comparing Figures 8(a) and 9(a), we see that the southern-hemisphere extension of the north polar hole has widened in the latitudinal direction after the lapse of a rotation; this might account for the increase in the wind speed from

~ 500 to ~ 600 km s⁻¹ at longitudes $\sim 270^\circ$ – 290° (compare Figures 8(d) and 9(d)). The pseudostreamer separatrix again runs nearly east–west and lies very close to the ecliptic plane over the longitude interval $\sim 225^\circ$ – 290° (Figure 9(c)). As indicated by Figure 9(d), the pseudostreamer is located on the trailing side of a high-speed stream. Between $\phi \sim 270^\circ$ and $\phi \sim 260^\circ$, v falls from ~ 600 to ~ 500 km s⁻¹ while O^{7+}/O^{6+}

2016 OCTOBER 29

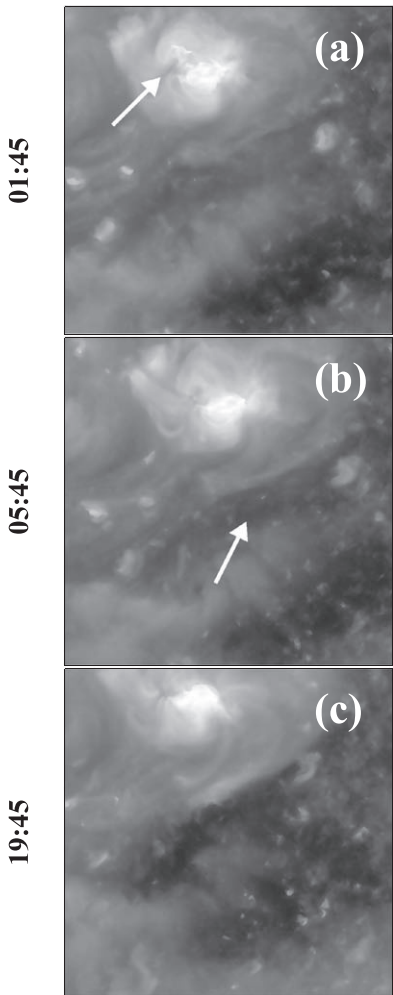


Figure 10. Sequence of Fe XIV 21.1 nm images recorded on 2016 October 29, showing an eruption in the newly emerged NOAA 12604, located at latitude $L \sim +6^\circ$. The small ejection or flare gives rise to a dimming front that propagates southwestward and merges with the nearby coronal hole. This event may have been responsible for the fluctuations in the IMF direction and O^{7+}/O^{6+} ratio seen near $\phi \sim 240^\circ$ in Figure 9(d).

remains $\lesssim 0.1$. Subsequently, as the wind speed decreases toward $\sim 400 \text{ km s}^{-1}$, the oxygen charge-state ratio and the IMF angle ϕ_B undergo large fluctuations. Some of this variability may have its origin in a small AR (NOAA 12604) which emerged near central meridian during October 26–29 and which may be seen at ($\phi \sim 260^\circ$, $L \sim +6^\circ$) in the Fe XIV map. Near 01:45 UTC on October 29, SDO EUV movies show a small ejective event occurring in the AR, followed by the formation of a dark front that propagates southwestward and eventually merges with the southern-hemisphere coronal hole (see Figure 10). Although we have been unable to identify an associated white-light CME, the observed perturbations of the hole boundaries are likely to have been accompanied by disturbances in the ecliptic wind.

Pseudostreamer separatrices are surrounded by narrow plasma sheets that extend outward from the cusp/X-point and contribute to the brightness of the outer white-light corona (see, e.g., Wang et al. 2007). Although these structures tend to be somewhat fainter than the corresponding extensions of helmet streamers, they may become easily visible when the

plasma sheet is oriented perpendicular to the sky plane. This is the case for the pseudostreamer of Figure 9, whose separatrix runs in the horizontal (east–west) direction over a range of longitudes centered at $\phi \sim 260^\circ$ (Figure 9(c)); the associated portion of the plasma sheet would thus be viewed edge-on when at the east or west limb.

To verify that the predicted pseudostreamer plasma sheet exists, we simulate the white-light streamer distribution during CR 2183 and compare the result with observations from the Large Angle and Spectrometric Coronagraph (LASCO) C2 instrument on the *Solar and Heliospheric Observatory (SOHO)*. Again applying a PFSS extrapolation to the WSO photospheric field to determine the boundaries between the different domains of the source-surface field, we calculate the sky-plane brightness patterns produced by Thomson scattering from plasma sheets that extend radially outward from the source-surface separatrices (for a more detailed description, see Wang et al. 2007). The top panels of Figure 11 show the WSO photospheric field and the separatrices at $r = R_{\text{ss}}$ during CR 2183 (as in Figure 9); the middle and bottom left panels display the LASCO east- and west-limb streamer patterns at $r \sim 4R_\odot$, while the middle and bottom right panels display the corresponding simulations. The white arrow indicates the location of the predicted pseudostreamer. A faint feature that straddles the ecliptic plane is visible at the corresponding position in the LASCO C2 maps.

4. Summary and Discussion

Using EUV observations of coronal holes and PFSS extrapolations of the photospheric field, we have identified 10 examples of Earth-directed pseudostreamers during 2013–2016 and searched for their signatures in the in situ solar wind. Some of these pseudostreamers were located between two equatorward excursions of the same polar coronal hole, or between the northern and southern parts of a transequatorial hole. Others separated pairs of like-polarity coronal holes on the same or opposite sides of the equator. In one case (Figures 5 and 6(a)–(b)), the pseudostreamer overlies a minority-polarity area within a transequatorial hole.

In regard to the solar wind observed in the vicinity of the predicted pseudostreamers, we were unable to identify any distinctive property that characterizes all of the encounters. The wind speeds varied over a large range (~ 320 – 600 km s^{-1}), with most of the speeds lying between ~ 400 and $\sim 550 \text{ km s}^{-1}$. The O^{7+}/O^{6+} ratios ranged from ~ 0.05 to ~ 0.35 and showed the expected inverse relation to speed.

Only in a subset of our cases (including that shown in Figure 4) was the pseudostreamer clearly associated with a stream interface. As remarked in the Introduction, a well-defined velocity dip/transition may be absent when the wind speeds from the leading coronal hole exceed or are comparable to those from the trailing hole.

Our finding that a wide range of wind speeds may be present in the vicinity of pseudostreamers does not support the idea that the pseudostreamers themselves are a major source of slow wind. If driven by random footpoint motions, interchange reconnection at the pseudostreamer cusp would be expected to give rise to low-speed wind on both sides of the separatrix between the open flux domains. Instead, fast wind is often observed on at least one side. In the 128 stream interfaces without polarity reversals studied by Crooker et al. (2014), the wind was (by selection) fast on the trailing side but slow on the leading side. We also note that low-speed wind is sometimes observed far from both pseudostreamers and sector boundaries,

WSO 2183 - OBSERVED & SIMULATED STREAMERS

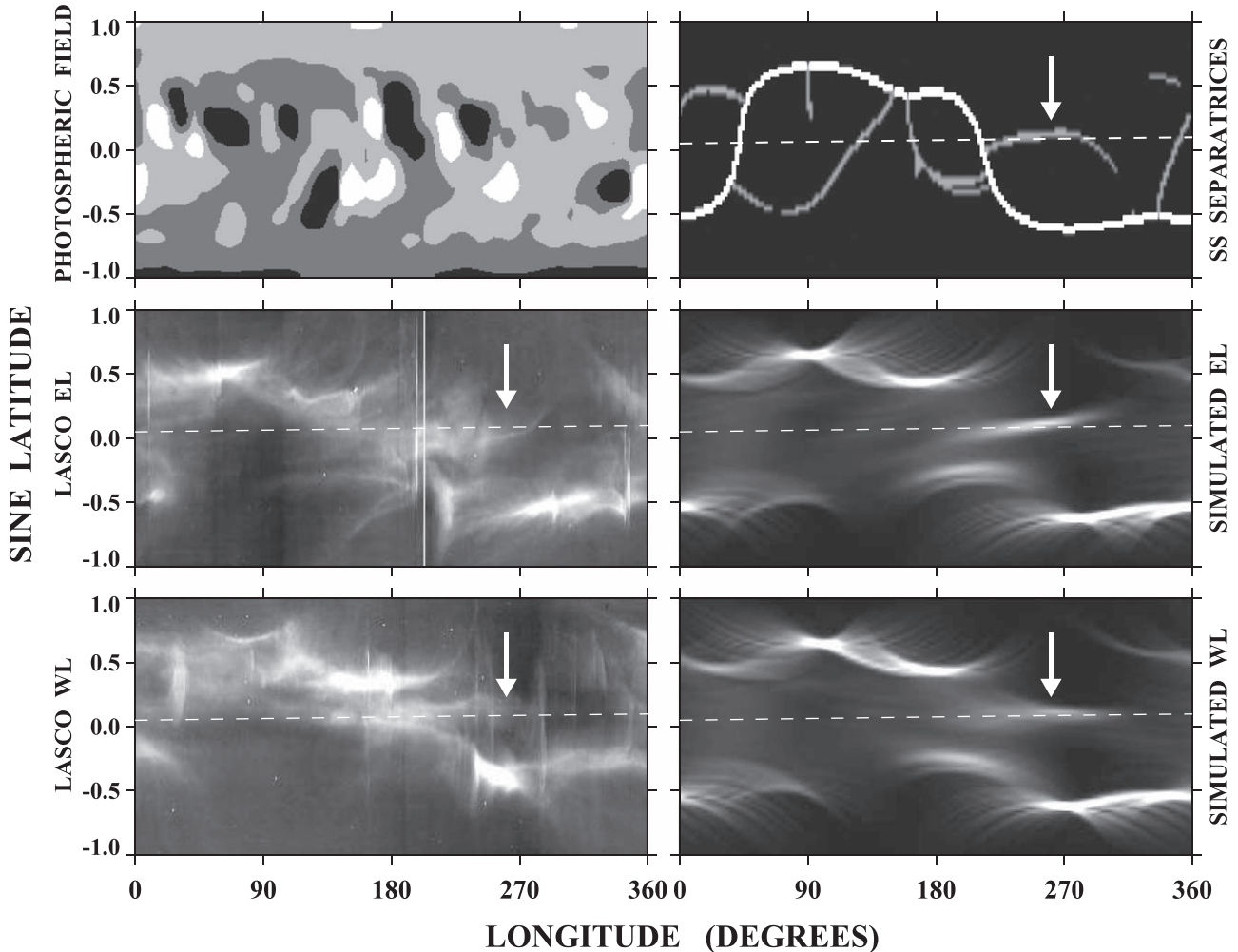


Figure 11. Observed and simulated coronal streamer structures during CR 2183 (starting date 2016 October 20). Top left: WSO photospheric field. Top right: boundaries between open flux domains at the source surface, with white pixels marking the neutral line (HCS) and gray pixels indicating the positions of pseudostreamer plasma sheets. Middle left: white-light streamer structures at $4 R_{\odot}$, recorded above the east limb by *SOHO/LASCO C2*. Middle right: simulated streamer patterns above the east limb. Bottom left: west-limb streamer structures recorded by LASCO C2 at $4 R_{\odot}$. Bottom right: simulated streamer patterns above the west limb. White arrows point to the location of the pseudostreamer in Figure 9.

as illustrated by Figure 3(d) (around $\phi \sim 270^\circ$). Indeed, the superposed epoch analysis of Crooker et al. (2014) shows that wind speeds $\lesssim 450 \text{ km s}^{-1}$ are typically present over a 4 day interval preceding the passage of the stream interface itself, both in the case of pseudostreamers and of helmet streamers (see their Figure 4).

An alternative explanation for the large range of wind speeds found near pseudostreamers is that the bulk of this wind comes from just inside the adjacent coronal holes, whose internal properties (including expansion factors and footpoint field strengths) determine the speed and composition of the wind. That both the fast and the slow wind originate from open field regions is already implicit in the use of the PFSS model. As may be seen from the plots of Section 3, the open flux tubes rooted next to Earth-directed pseudostreamers show a wide variety of divergence rates, with the values of f_{\max} (indicated by the color-coded diamonds) tending to be inversely correlated with the observed wind speeds. Thus, in Figures 1–4, the pseudostreamer crossings where $v \lesssim 400 \text{ km s}^{-1}$ have $f_{\max} > 9$ (green and blue diamonds); conversely, in Figures 7–9, the

crossings (near $\phi \sim 270^\circ$) where $v \sim 500\text{--}600 \text{ km s}^{-1}$ have $f_{\max} < 9$ (yellow and orange diamonds). However, it should be emphasized that a single parameter such as f_{\max} cannot adequately represent the effect of the highly nonmonotonic expansion occurring in the vicinity of the pseudostreamer cusp (see Wang et al. 2012; Panasenco & Velli 2013; Panasenco et al. 2019).

Although interchange reconnection between pseudostreamers and the adjacent coronal-hole flux is unlikely to be a major source of slow wind, this process may well account for their plasma sheet extensions. These narrow structures are seen in projection in the white-light corona and undoubtedly provide a small contribution to the slow wind. However, interactions with the surrounding medium during the transit to 1 au make it difficult to distinguish the in situ signatures of the pseudostreamer (and helmet streamer) plasma sheets.

As suggested by the fluctuations in the IMF angle and the O^{7+}/O^{6+} ratio near $\phi \sim 240^\circ$ in Figure 9(d) and by Figure 10, small transient events in ARs may be a source of highly variable slow wind. Such events may produce unsteady

conditions in the solar wind even in the absence of identifiable white-light or interplanetary CMEs.

Our use of near-Earth measurements to infer the properties of the solar wind around pseudostreamers has obvious limitations. During the propagation from the Sun to 1 au, the spatial and temporal variations in speed, density, and composition are modified. Interactions between fast and slow wind are particularly prevalent in the ecliptic plane, flattening the gradients that may have originally been present near the pseudostreamer boundaries. Moreover, the number of cases studied here is too small to allow us to draw general conclusions about the nature of pseudostreamer-associated wind. As mentioned earlier, the largest and longest-lived pseudostreamers are not located near the equator, but are rooted between the sunspot latitudes and the polar hole in each hemisphere. The upcoming *Solar Orbiter* mission, as well as the *Parker Solar Probe*, may enable us to overcome at least some of these problems and provide a better understanding of the solar wind in the vicinity of pseudostreamers.

We are indebted to L. Huttig for providing the AIA and LASCO synoptic maps used in this paper. This work was supported by the NASA H-GI/Open, NASA SPP, and NOAA/NASA HSWO2R programs and by the Chief of Naval Research.

ORCID iDs

Y.-M. Wang  <https://orcid.org/0000-0002-3527-5958>

References

- Abbo, L., Lionello, R., Riley, P., & Wang, Y.-M. 2015, *SoPh*, 290, 2043
 Abbo, L., Ofman, L., Antiochos, S. K., et al. 2016, *SSRv*, 201, 55
 Antiochos, S. K., Mikić, Z., Titov, V. S., Lionello, R., & Linker, J. A. 2011, *ApJ*, 731, 112
 Arge, C. N., & Pizzo, V. J. 2000, *JGR*, 105, 10465
 Cohen, O. 2015, *SoPh*, 290, 2245
 Cranmer, S. R., van Ballegooijen, A. A., & Edgar, R. J. 2007, *ApJS*, 171, 520
 Crooker, N. U., Antiochos, S. K., Zhao, X., & Neugebauer, M. 2012, *JGR*, 117, A04104
 Crooker, N. U., & McPherron, R. L. 2012, *JGR*, 117, A09104
 Crooker, N. U., McPherron, R. L., & Owens, M. J. 2014, *JGRA*, 119, 4157
 Del Zanna, G., & Bromage, B. J. I. 1999, *JGR*, 104, 9753
 Eselevich, V. G., Fainshtein, V. G., & Rudenko, G. V. 1999, *SoPh*, 188, 277
 Higgins, A. K., Antiochos, S. K., DeVore, C. R., Wyper, P. F., & Zurbuchen, T. H. 2017a, *ApJ*, 837, 113
 Higgins, A. K., Antiochos, S. K., DeVore, C. R., Wyper, P. F., & Zurbuchen, T. H. 2017b, *ApJL*, 840, L10
 Higgins, A. K., & Lynch, B. J. 2018, *ApJ*, 859, 6
 Levine, R. H., Altschuler, M. D., & Harvey, J. W. 1977, *JGR*, 82, 1061
 Neugebauer, M., Liewer, P. C., Goldstein, B. E., Zhou, X., & Steinberg, J. T. 2004, *JGR*, 109, A10102
 Owens, M. J., Crooker, N. U., & Lockwood, M. 2014, *JGRA*, 119, 36
 Panasenco, O., & Velli, M. 2013, in AIP Conf. Proc. 1539, Solar Wind 13, ed. G. P. Zank et al. (Melville, NY: AIP), 50
 Panasenco, O., Velli, M., & Panasenco, A. 2019, *ApJ*, in press
 Poduval, B. 2016, *ApJL*, 827, L6
 Pontin, D. I., & Wyper, P. F. 2015, *ApJ*, 805, 39
 Rappazzo, A. F., Matthaeus, W. H., Ruffolo, D., Servidio, S., & Velli, M. 2012, *ApJL*, 758, L14
 Riley, P., & Luhmann, J. G. 2012, *SoPh*, 277, 355
 Rouillard, A. P., Davies, J. A., Lavraud, B., et al. 2010, *JGR*, 115, A04103
 Schwadron, N. A., Fisk, L. A., & Zurbuchen, T. H. 1999, *ApJ*, 521, 859
 Sheeley, N. R., Jr., Lee, D. D.-H., Casto, K. P., Wang, Y.-M., & Rich, N. B. 2009, *ApJ*, 694, 1471
 Timothy, A. F., Krieger, A. S., & Vaiana, G. S. 1975, *SoPh*, 42, 135
 Wang, Y.-M. 2017, *ApJ*, 841, 94
 Wang, Y.-M., Grappin, R., Robbrecht, E., & Sheeley, N. R., Jr. 2012, *ApJ*, 749, 182
 Wang, Y.-M., Ko, Y.-K., & Grappin, R. 2009, *ApJ*, 691, 760
 Wang, Y.-M., & Sheeley, N. R., Jr. 1990, *ApJ*, 355, 726
 Wang, Y.-M., & Sheeley, N. R., Jr. 1992, *ApJ*, 392, 310
 Wang, Y.-M., & Sheeley, N. R., Jr. 1993, *ApJ*, 414, 916
 Wang, Y.-M., & Sheeley, N. R., Jr. 1995, *ApJL*, 447, L143
 Wang, Y.-M., & Sheeley, N. R., Jr. 2003, *ApJ*, 587, 818
 Wang, Y.-M., & Sheeley, N. R., Jr. 2004, *ApJ*, 612, 1196
 Wang, Y.-M., Sheeley, N. R., Jr., & Rich, N. B. 2007, *ApJ*, 658, 1340
 Wang, Y.-M., Sheeley, N. R., Jr., Walters, J. H., et al. 1998, *ApJL*, 498, L165
 Zhao, L., Zurbuchen, T. H., & Fisk, L. A. 2009, *GeoRL*, 36, L14104
 Zhao, X. P., Hoeksema, J. T., & Scherrer, P. H. 1999, *JGR*, 104, 9735
 Zurbuchen, T. H., Hefti, S., Fisk, L. A., Gloeckler, G., & Schwadron, N. A. 2000, *JGR*, 105, 18327